Supporting Information

Boosted Charge Transfer in Twinborn α-(Mn_2O_3-MnO_2) Heterostructures: Toward High Rate and Ultralong Life Zinc-ion Batteries

Jun Long, [†,‡] Fuhua Yang, [‡] Jing Cuan, [‡] Jingxing Wu, [‡] Zhanhong Yang, [*,†] Hao Jiang, [§] Rui Song, [∥] Wenlong Song, [∥] Jianfeng Mao, [*,‡] Zaiping Guo [‡]

[†]Hunan Provincial Key Laboratory of Chemical Power Sources, College of Chemistry and Chemical Engineering, Central South University, Changsha 410083, P. R. China

[‡]Institute for Superconducting & Electronic Materials, Australian Institute for Innovative Materials (AIIM), School of Mechanical, Materials, Mechatronics and Biomedical Engineering, University of Wollongong, Wollongong, New South Wales 2522, Australia

[§]Center of Super-Diamond and Advanced Films (COSDAF) & Department of Materials Science and Engineering, City University of Hong Kong, Tat Chee Avenue, Kowloon, Hong Kong 999077, China

[∥]Tianneng Battery Group Co Ltd, Zhejiang 313100, China

[*]E-mail: zhyang@csu.edu.cn

[*]E-mail: jmao@uow.edu.au

The pseudocapacitive effect calculation

The pseudocapacitive effects could be analyzed according to the relationship between the peak currents and the scan rates, which are acquired from the CV curves [1, 2]:

$$i = av^b \qquad (1)$$

where *a* and *b* are the adjustable constants. The *b*-value of 0.5 suggests a diffusion-controlled process, while *b* is close to 1.0 indicates a capacitive process, which is determined from slope of the log *i* versus log *v* plots. Furthermore, the contributions to the capacity can be quantified [3] by the equation (2):

$$i(v) = k_1 v + k_2 v^{1/2} \qquad (2)$$

where k_1v and $k_2v^{1/2}$ represent the pseudocapacitive and diffusion-dominant contributions, respectively.

Zn^{2+} diffusion coefficient (D_{Zn}) calculation

Electrochemical impedance spectroscopy (EIS) measurement is adopted to investigate the reaction kinetics for the zinc ion batteries (ZIBs) within the frequency range from 100 kHz to 0.01 Hz. The relevant Nyquist plots are exhibited in Fig. S7(a). Obviously, all the patterns show the similar shape with the semicircle (at high frequency region) and the inclined straight line (at low frequency region), indicating that electrochemical process is regulated by the charge transfer and the ion diffusion [4]. The R_{ct} values of α-(Mn_2O_3@MnO_2)-400, α-(Mn_2O_3@MnO_2)-450, α-(Mn_2O_3@MnO_2)-500 electrodes are 297.2 Ω, 237.7 Ω and 175.6 Ω, respectively.

Additionally, the diffusion coefficient of the Zn^{2+} (D_{Zn}) in the electrode can be calculated with the low frequency region of the EIS plots (as shown in Fig. S7(b)) according to the following equation [5]:

$$D = \frac{R^2T^2}{2A^2n^4F^4C^2\sigma^2} \qquad (3)$$

Where the meaning of n is the number of the electrons per molecule, R the gas constant, T the absolute temperature, A the surface area of the electrode, F the Faraday constant, C the concentration of the Zn^{2+}, σ is the Warburg factor which has relationship with Z_{re}:

$$Z_{re} = R_D + R_L + \sigma\omega^{1/2} \qquad (4)$$

The relationships between Z_{re} and $\omega^{1/2}$ (the square root of the frequency) are shown in Fig. S7(b) in the low frequency region. The D_{Zn} is obtained based on the equations (3) and (4).

GITT measurements and the calculation of the D_{Zn} calculation

Based on the GITT tests, the D_{Zn} in the electrodes can be determined by solving Fick's second law [6-8] with Equation (5) based on the GITT curves.

$$D = \frac{4}{\pi\tau}\left(\frac{m_aV_M}{M_aS}\right)^2\left(\frac{\Delta E_S}{\Delta E_\tau}\right)^2 \qquad (5)$$

where m_a is the electrode active mass, M_a is the molar mass of the electrode material (g/mol) and V_M is the molar volume (cm^3/mol), S is the geometric area of the electrode (contacting area of the electrode with electrolyte), ΔE_S is the difference in the open circuit voltage measured at the end of the relaxation period for the two successive steps, and ΔE_τ is the slope of the linearized region of the potential during the current

pulse of the duration time. In our work, the equation is simplified on the condition that the $\Delta E_\tau/\tau^{1/2}$ shows a linear relationship. Before the GITT measurement, the assembled cells are first charged/discharged at 50 mA g^{-1} for one cycle to stabilize the cells. The current pulse lasts for 30 min at 100 mA g^{-1} and then the cells are relaxed for 1 h to make the voltage reach the equilibrium. And these procedures are repeatedly applied to the cells during the total discharge/charge process.

Theoretical Calculations

All the spin theoretical simulations in our work were carried out on the Vienna ab initio Simulation Package (VASP) with the version 5. 4. 1 [9]. The Generalized gradient approximation (GGA) with the Perdew-Burke-Emzerhof (PBE) [10] functional form is employed to evaluate the electron-electron exchange and correlation interactions while the projector augmented-wave (PAW) methods [11] are implanted to represent the core-electron (valence electron) interactions. The GGA + U [12] calculations are performed with the on-site Coulomb repulsion U term on the Mn 3d and the U_{eff} ($U_{eff} = U - J$) values are 4.5 eV [13], respectively. Plane-Wave basis function is set with a kinetic cut-off energy of 400 eV. The ground-state atomic geometries are optimized by relaxing the force below 0.02 eV/Å and the convergence criteria for energy is set with the value of 1.0×10^{-5} eV/cell. Only Gamma point of $1 \times 1 \times 1$ in the Brillouin zone are considered for our calculations. Gaussian method is employed for the both electronic structures and total energy of our models and stress/force relaxations.

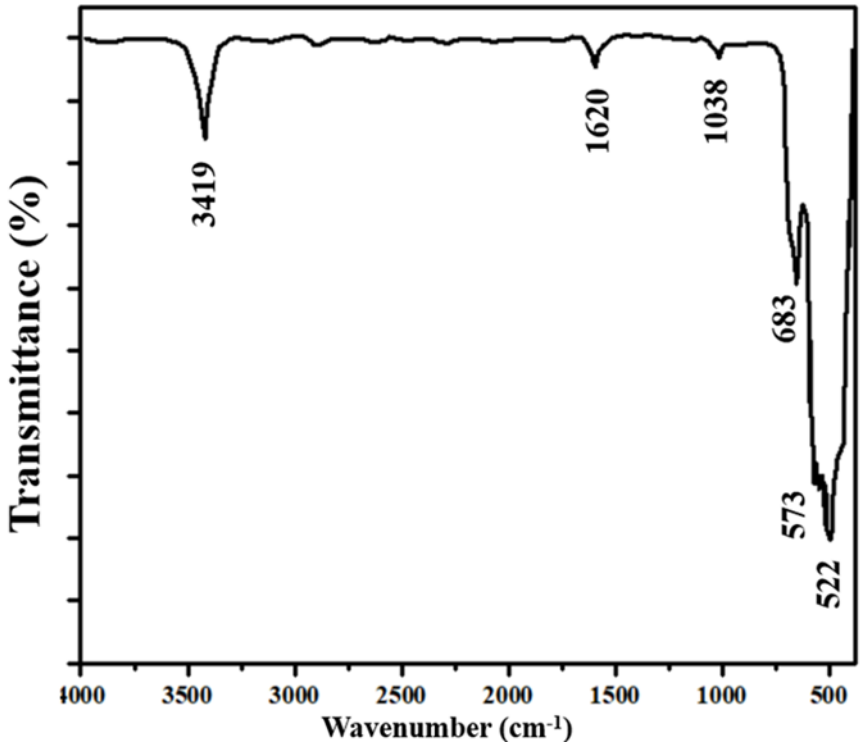

Figure S1. FT-IR spectra of bare α-(Mn_2O_3-MnO_2)-500.

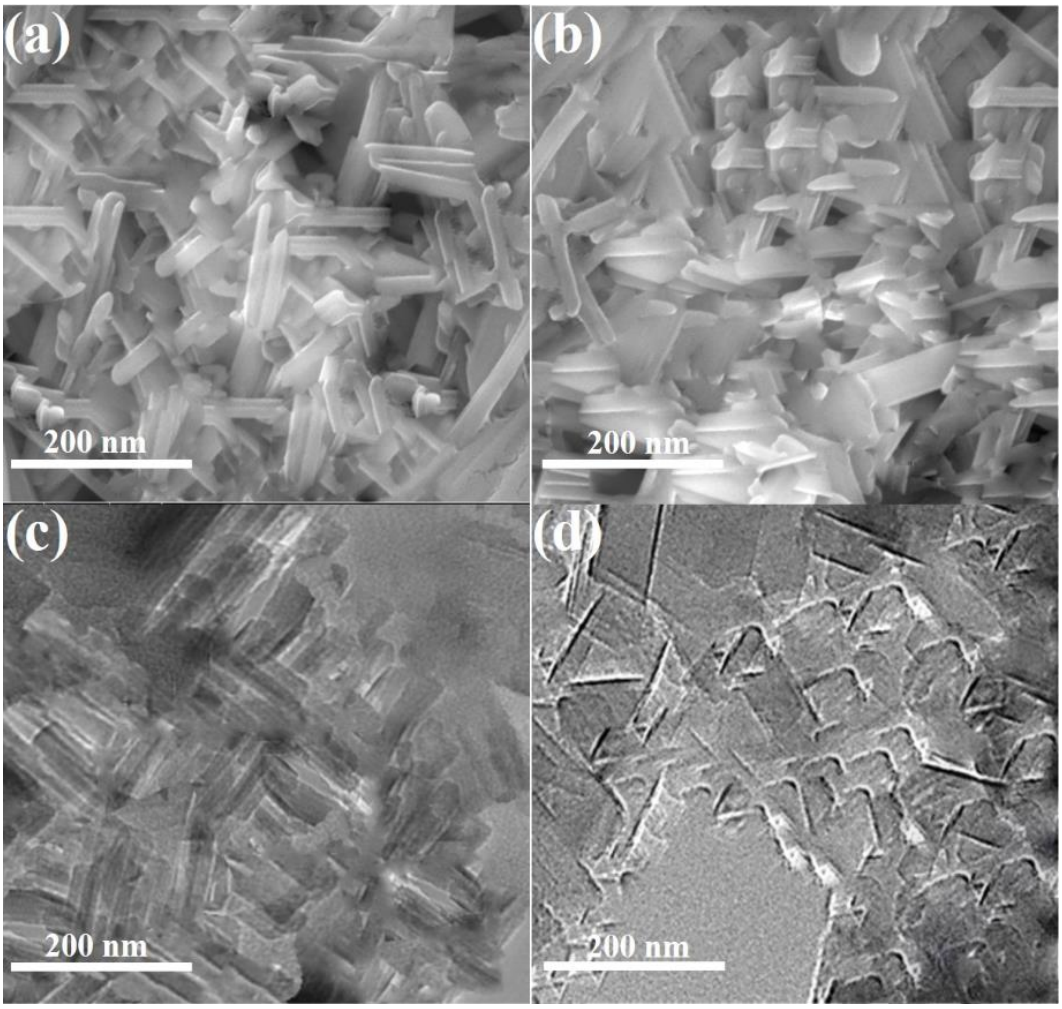

Figure S2. SEM images of the α-(Mn_2O_3-MnO_2)-550 (a), α-(Mn_2O_3-MnO_2)-600 (b). TEM images of the α-(Mn_2O_3-MnO_2)-550 (c) and α-(Mn_2O_3-MnO_2)-600 (d).

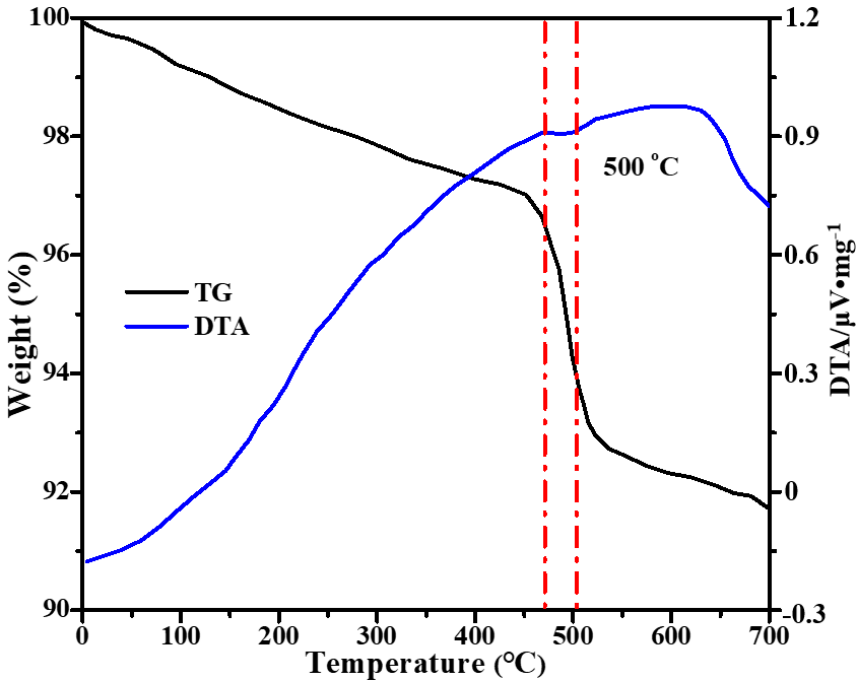

Figure S3. TG and DTA profiles of the precursor of α-(Mn_2O_3-MnO_2)-500.

(a)

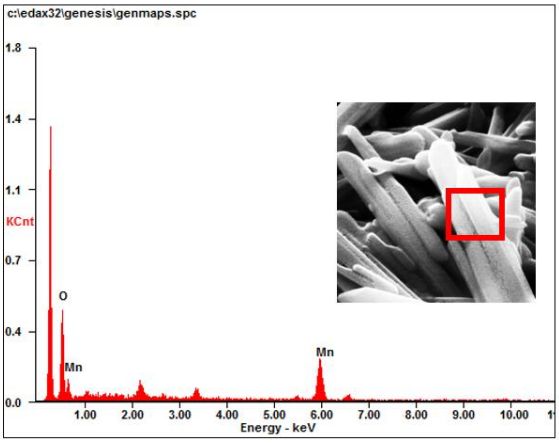

(b)

Element	Wt%	At%
OK	33.57	63.44
MnK	66.43	36.56
Matrix	Correction	ZAF

Figure S4. (a) EDS image and (b) the element concentration of the α-(Mn_2O_3-MnO_2)-500.

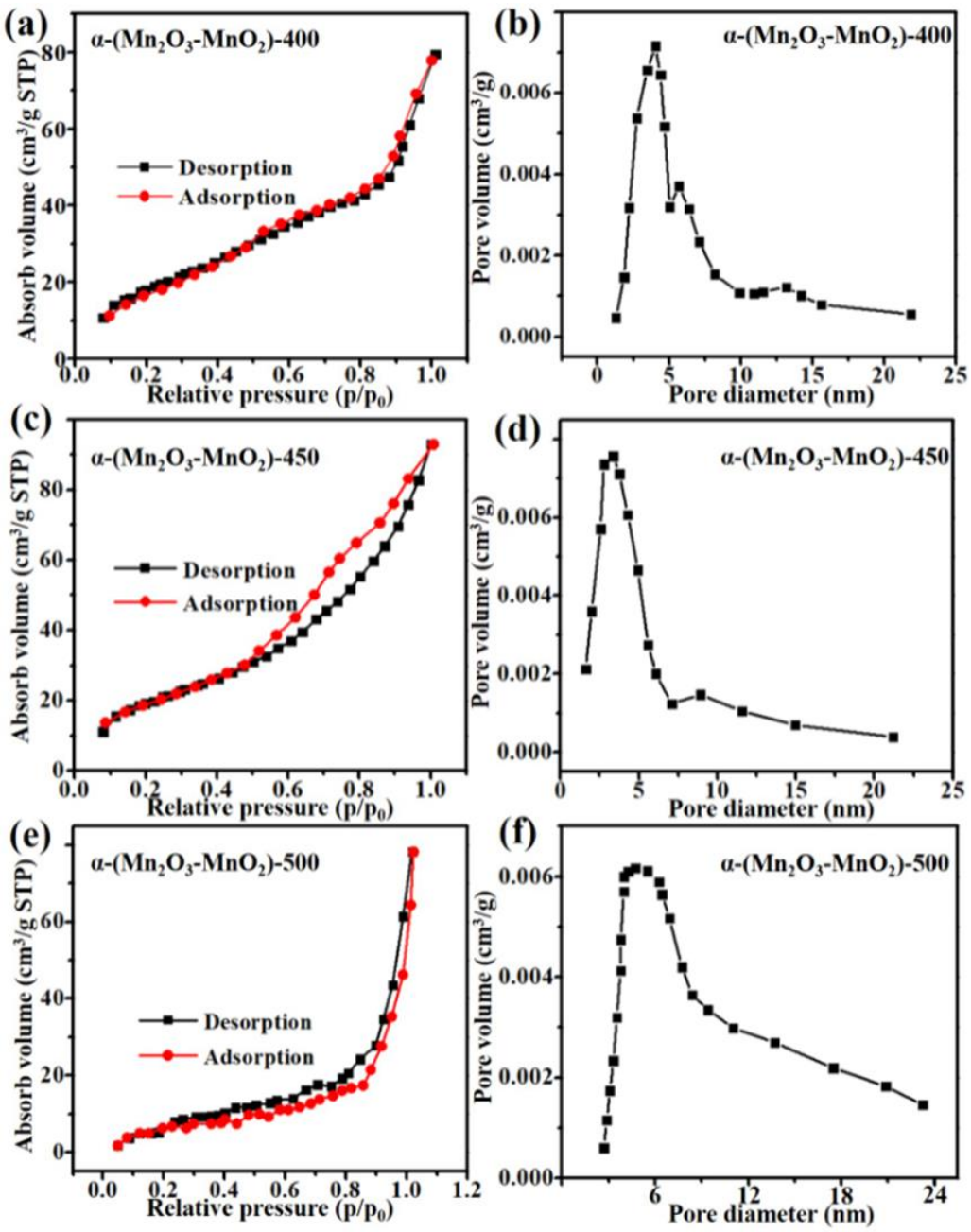

Figure S5. Nitrogen adsorption/desorption isotherms of the α-(Mn_2O_3-MnO_2)-400 (a), α-(Mn_2O_3-MnO_2)-450 (c) and α-(Mn_2O_3-MnO_2)-500 (e). The corresponding BJH pore size distributions of the α-(Mn_2O_3-MnO_2)-400 (b), α-(Mn_2O_3-MnO_2)-450 (d) and α-(Mn_2O_3-MnO_2)-500 (f).

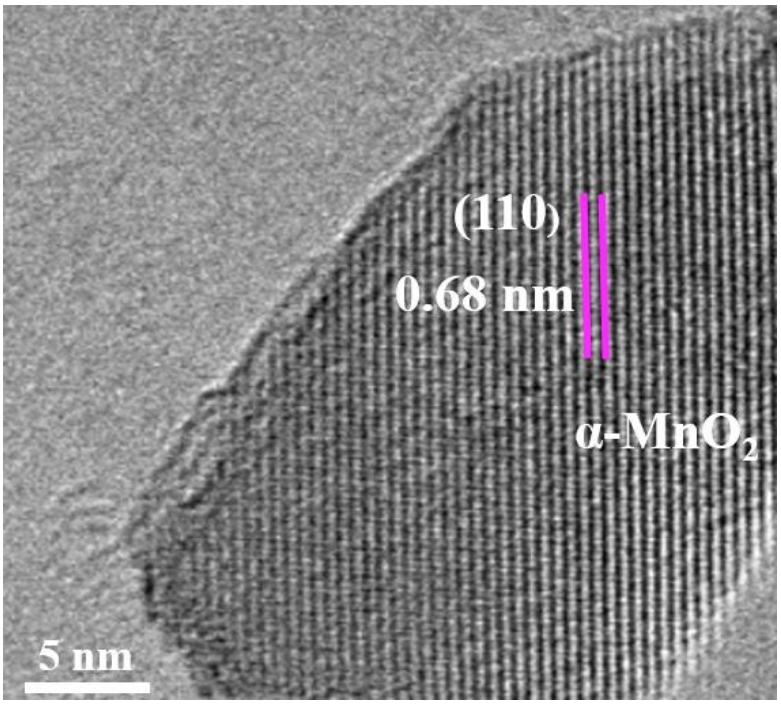

Figure S6. HRTEM images of the α-(Mn_2O_3-MnO_2)-450.

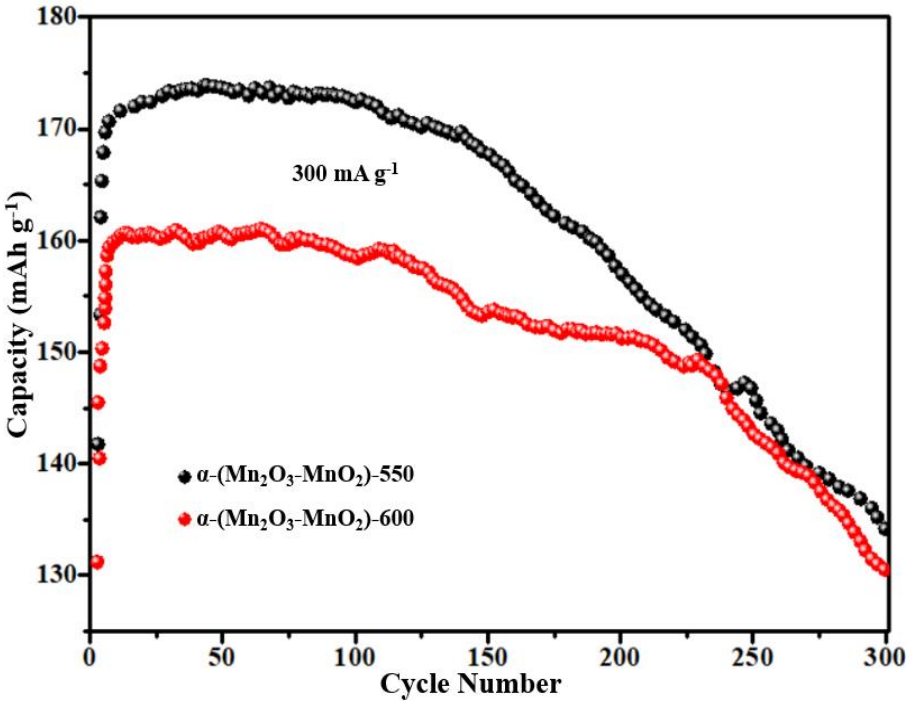

Figure S7. Cycle performance of α-(Mn_2O_3-MnO_2)-550 and α-(Mn_2O_3-MnO_2)-600 electrodes at current density of 300 mA g^{-1}.

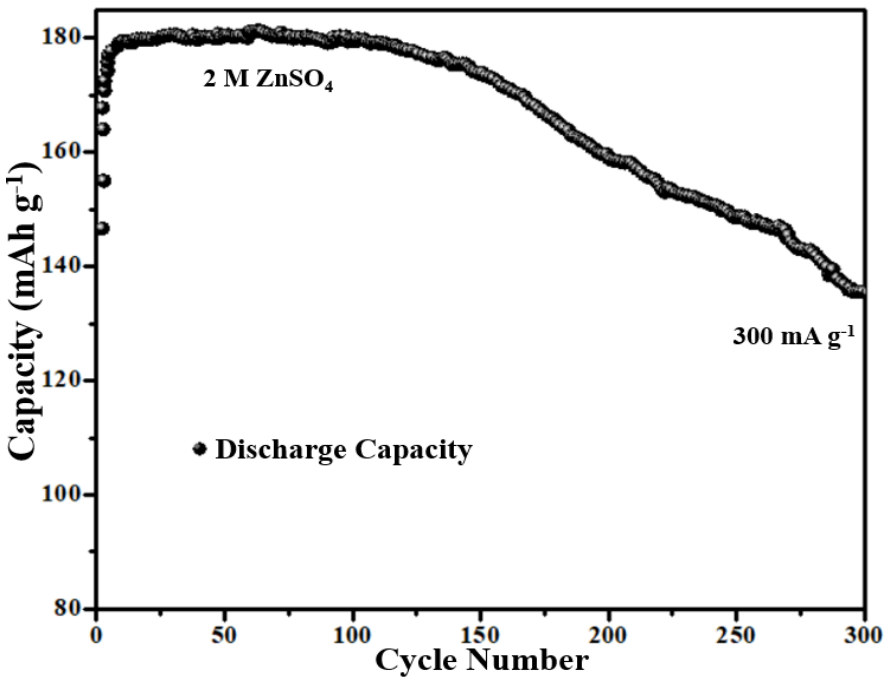

Figure S8. Cycle performance of α-(Mn_2O_3-MnO_2)-500 electrode at current density of 300 mA g^{-1} in 2 M $ZnSO_4$ electrolyte.

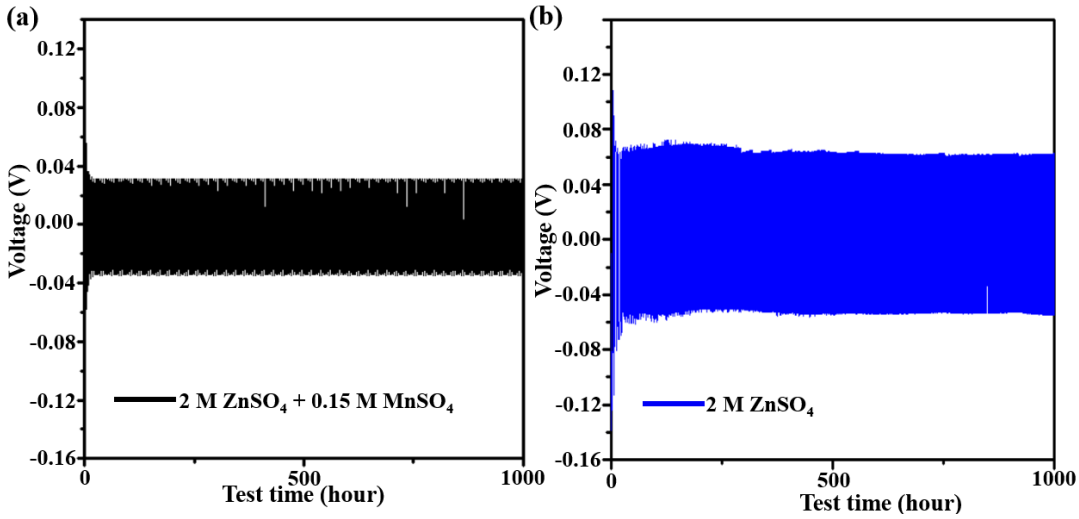

Figure S9. (a) Long-term cycling performance of Zn/Zn symmetrical cells in 2 M $ZnSO_4$ + 0.15 M $MnSO_4$ and (b) 2 M $ZnSO_4$ electrolytes.

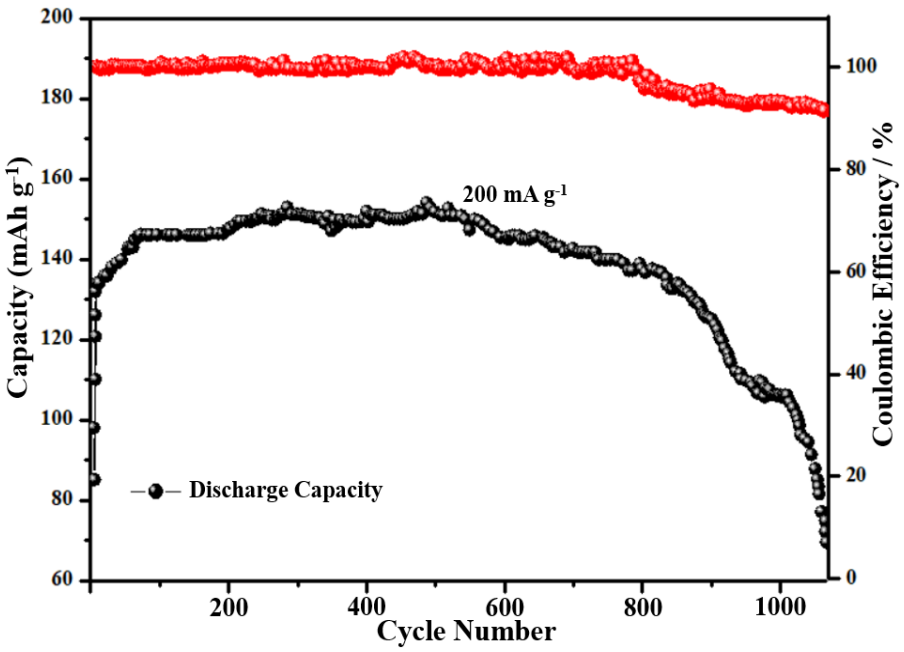

Figure S10. Cycle performance of α-Mn_2O_3 electrode at 200 mA g^{-1}.

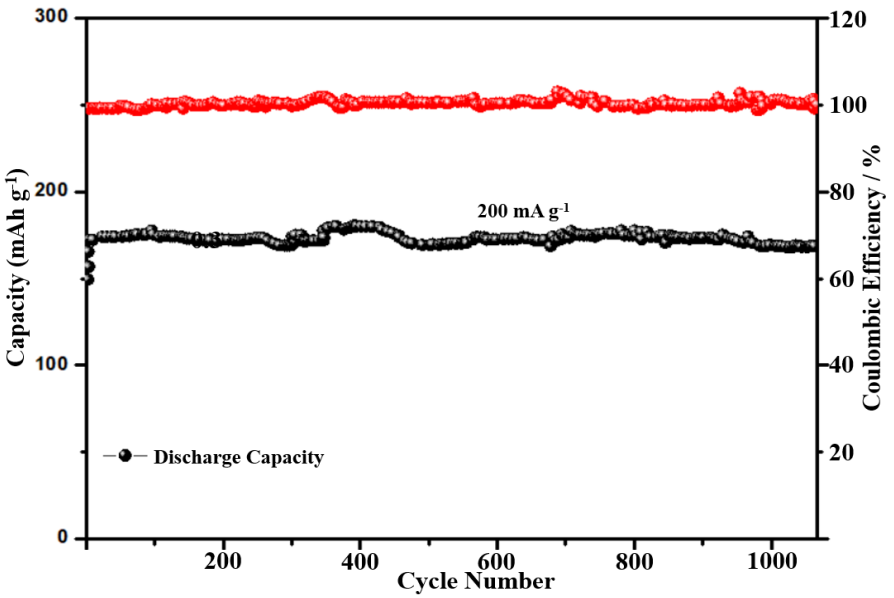

Figure S11. Cycle performance of α-(Mn_2O_3-MnO_2)-500 electrode at current density of 200 mA g^{-1}.

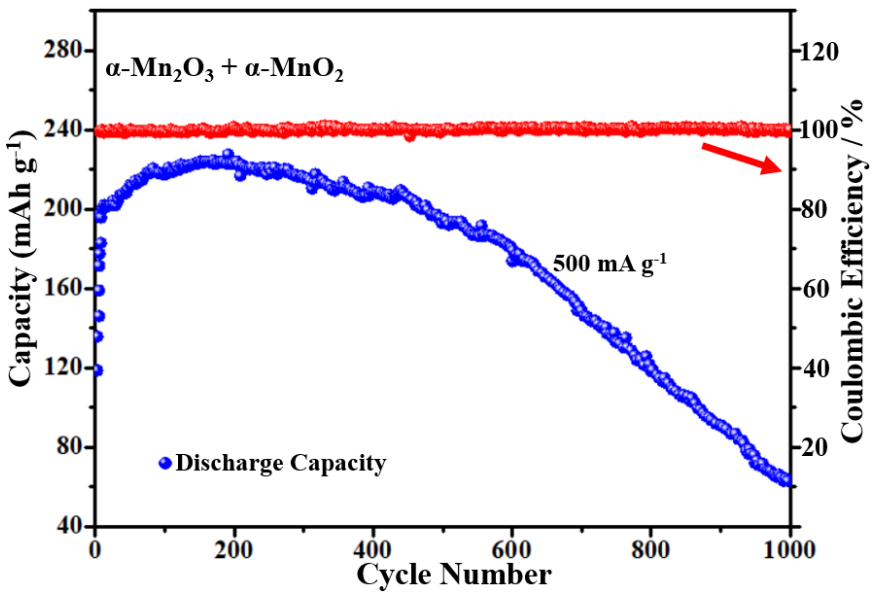

Figure S12. Cycle performance of α-Mn_2O_3+α-MnO_2 mixture at current density of 500 mA g^{-1}.

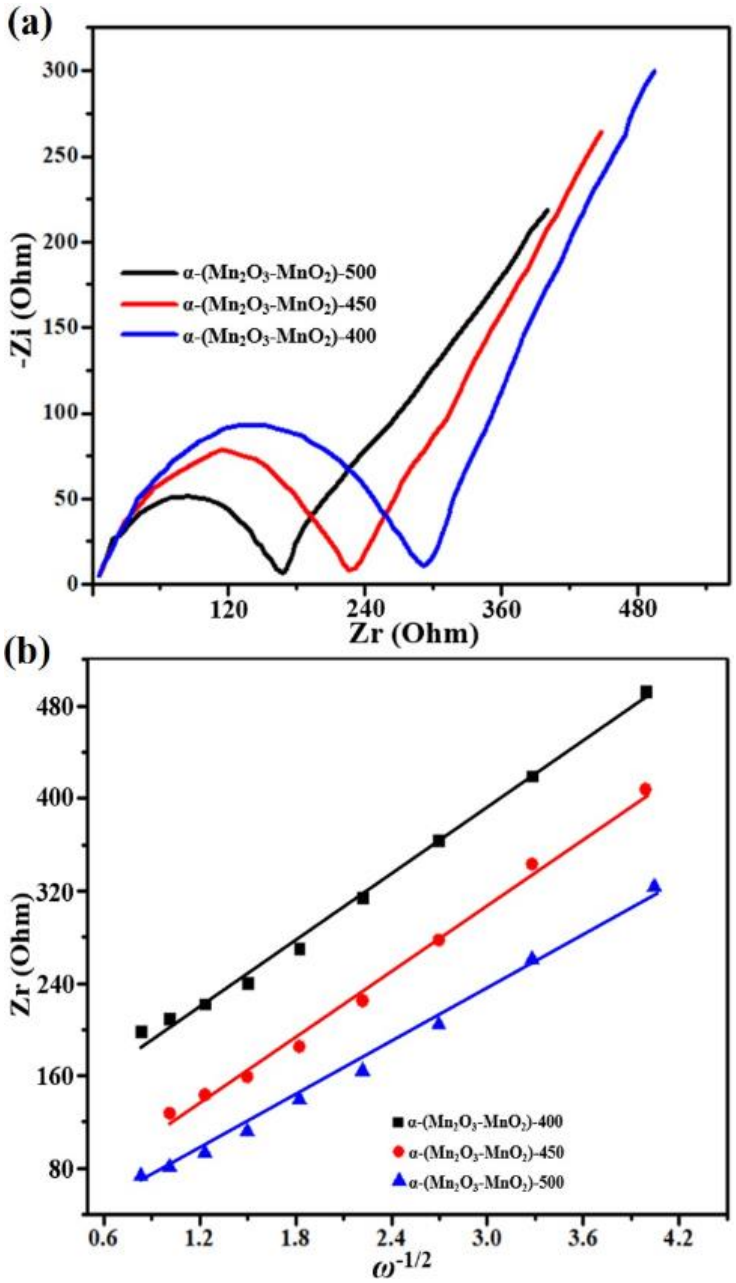

Figure S13. (a) EIS for α-(Mn_2O_3-MnO_2)-400, α-(Mn_2O_3-MnO_2)-450, α-(Mn_2O_3-MnO_2)-500 electrodes after the first discharge at 500 mA g^{-1}. (b) The linear relationship between Z' and $\omega^{-1/2}$ of the α-(Mn_2O_3-MnO_2)-400, α-(Mn_2O_3-MnO_2)-450, α-(Mn_2O_3-MnO_2)-500 electrodes in the low frequency region.

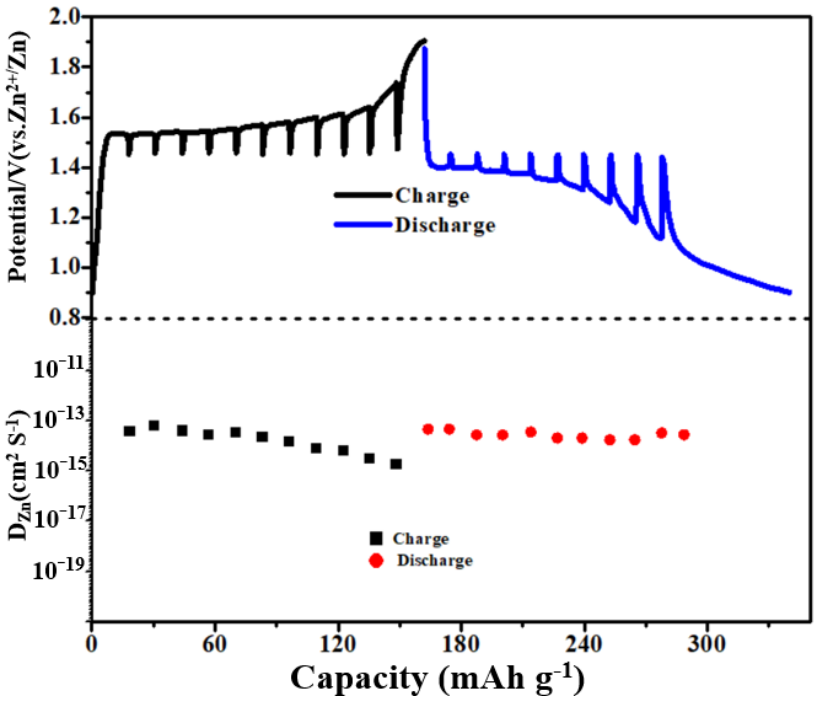

Figure S14. GITT profile and calculated D_{Zn} of α-(Mn_2O_3-MnO_2)-500 electrode.

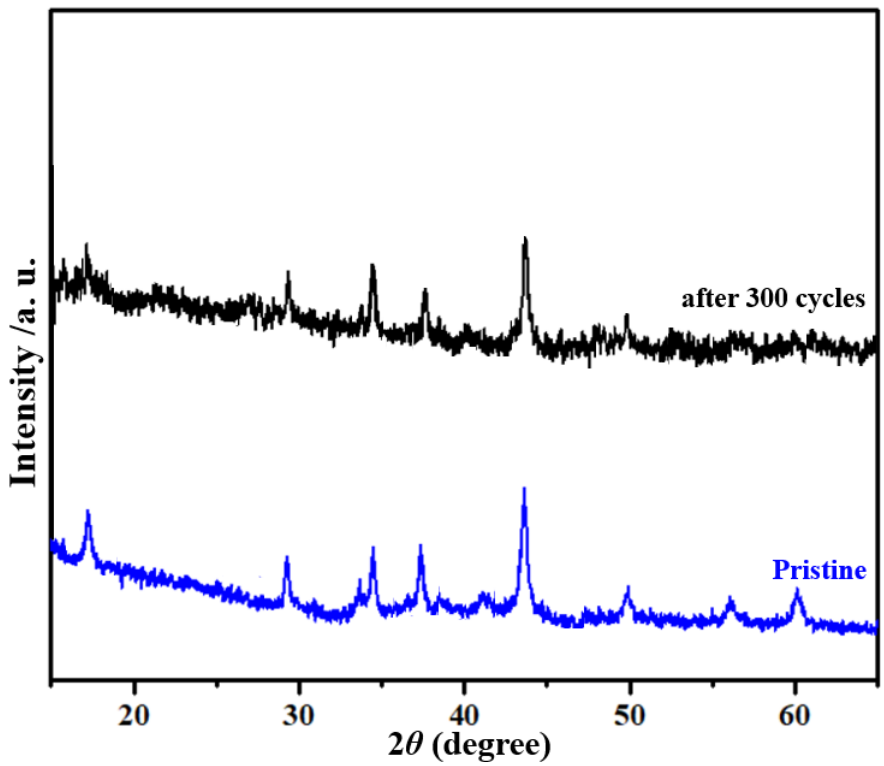

Figure S15. XRD patterns of α-(Mn_2O_3@MnO_2)-500 electrode at pristine state and after 300 cycles at current density of 300 mA g^{-1}.

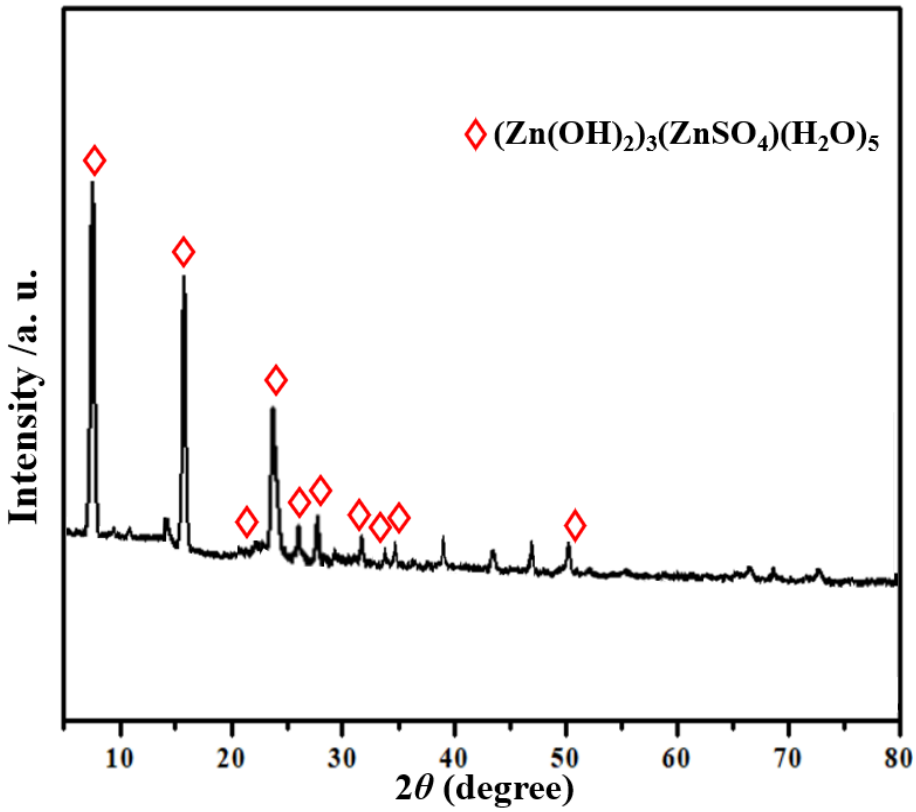

Figure S16. XRD pattern of α-(Mn_2O_3-MnO_2)-500 cathode in the 10th discharged state.

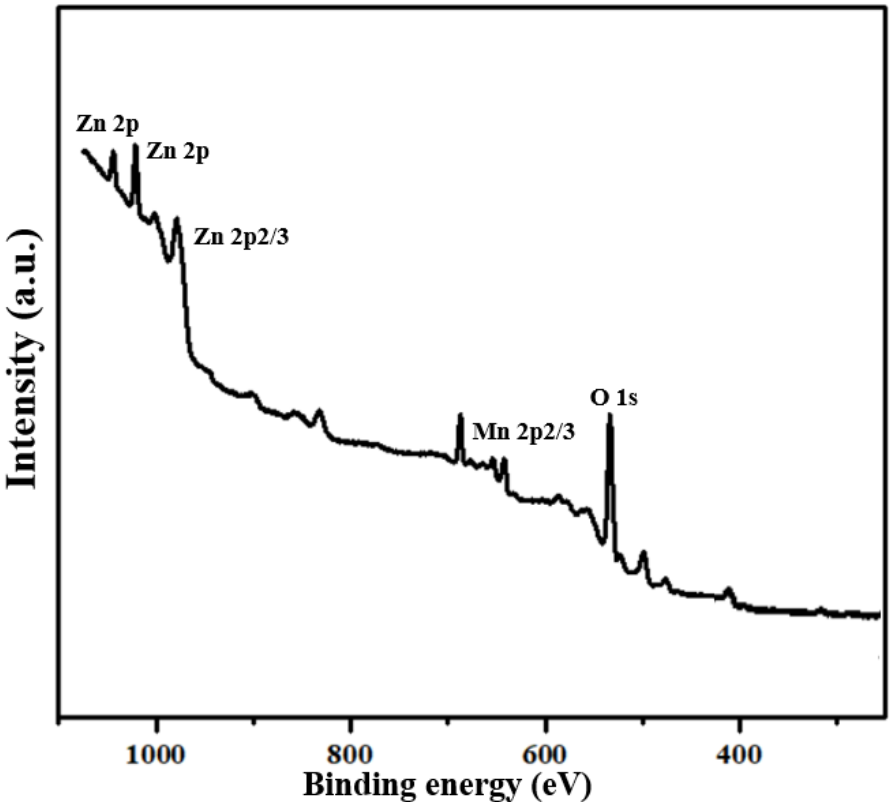

Figure S17. XPS spectra of survey spectrum of the α-(Mn_2O_3-MnO_2)-500 electrode at discharge state during the first cycle of the zinc ion battery.

Table S1. Zn^{2+} storage performance of α-(Mn_2O_3-MnO_2)-500 compared with

previously reported materials.

Materials	**High rate capacity**	**Cycling performance**	**Electrolyte**	**Ref.**
α-(Mn_2O_3-MnO_2)-500	180.5 mAh g^{-1} at 100 mA g^{-1} 123.7 mAh g^{-1} at 1500 mA g^{-1}	170 mA g^{-1} after 2000 cycles at 500 mAh g^{-1}	2 M $ZnSO_4$ + 0.15 M $MnSO_4$	This work
amorphous α-MnO_2	210 mAh g^{-1} at 105 mA g^{-1} 121 mAh g^{-1} at 1500 mA g^{-1}	100 mAh g^{-1} after 100 cycles at 105 mA g^{-1}	1 M $ZnSO_4$	[14]
α-MnO_2 nanorod	/	140 mAh g^{-1} after 30 cycles at 42 mA g^{-1}	1 M $ZnSO_4$	[15]
Todorokite-type MnO_2	90 mAh g^{-1} at 90 mA g^{-1} 42 mAh g^{-1} at 900 mA g^{-1}	98 mAh g^{-1} after 100 cycles at 60 mA g^{-1}	1 M $ZnSO_4$	[16]
$Zn_3[Fe(CN)_6]_2$	67 mAh g^{-1} at 60 mA g^{-1} 53 mAh g^{-1} at 1500 mA g^{-1}	81 mAh g^{-1} after 100 cycles at 60 mA g^{-1}	1 M $ZnSO_4$	[17]
$Cu_3[Fe(CN)_6]_2$	48 mAh g^{-1} at 150 mA g^{-1} 43 mAh g^{-1} at 600 mA g^{-1}	52 mAh g^{-1} after 100 cycles at 60 mA g^{-1}	20 mM $ZnSO_4$	[18]
Mesoporous γ-MnO_2	/	150 mAh g^{-1} after 100 cycles at 0.5 mA cm^{-2}	1 M $ZnSO_4$	[19]
Spinel-$ZnMn_{1.86}O_4$	/	150 mAh g^{-1} after 50 cycles at 50 mA g^{-1}	3 M $Zn(CF_3SO_3)_2$	[20]
$Na_3V_2(PO_4)_3$	97 mAh g^{-1} at 50 mA g^{-1} 62 mAh g^{-1} at 1000 mA	108 mAh g^{-1} after 200 cycles at 100	0.5 M $Zn(CH_3COO)_2$	[21]

	g^{-1}	mA g^{-1}		
zinc orthovanadate	201 mAh g^{-1} at 200 mA g^{-1} 165 mAh g^{-1} at 1000 mA g^{-1}	125 mA h g^{-1} after 800 cycles at 2000 mA g^{-1}	1 M $Zn(TFSI)_2$ + 20 M LiTFSI	[22]
$V_{10}O_{24}\cdot 12H_2O$	164.5 mAh g^{-1} at 200 mA g^{-1} 118.5 mAh g^{-1} at 1000 mA g^{-1}	98 mAh g^{-1} after 500 cycles at 10 A g^{-1}	3 M $Zn(CF_3SO_3)_2$	[23]
V_2O_5	100 mAh g^{-1} at 1000 mA g^{-1} 92 mAh g^{-1} at 2000 mA g^{-1}	121 mAh g^{-1} after 400 cycles at 1000 mA g^{-1}	3 M $ZnSO_4$	[24]
KMn_8O_{16}	130 mAh g^{-1} at 100 mA g^{-1}	77 mAh g^{-1} after 100 cycles at 100 mA g^{-1}	1 M $ZnSO_4$ + 0.3 M K_2SO_4	[25]
$Na_{1.1}V_3O_{7.9}$ nanoribbons/graphene	170 mA h g^{-1} at 100 mA g^{-1} 100 mAh g^{-1} at 1 A g^{-1}	84.8 mAh g^{-1} after 500 cycles at 1000 mA g^{-1}	1 M $Zn(CF_3SO_3)_2$	[26]
3D MnO_x@C	190 mA h g^{-1} at 300 mA g^{-1} 75 mAh g^{-1} at 1.5 A g^{-1}	60 mA h g^{-1} after 1000 cycles at 2000 mA g^{-1}	0.75 M Na2SO4 + 0.25 M ZnSO4	[27]
$ZnMn_2O_4/Mn_2O_3$	82.6 mA h g^{-1} at 500 mA g^{-1} 42.1 mA h g^{-1} at 3.2 A g^{-1}	111.9 mAh g^{-1} after 300 cycles at 0.5 A g^{-1}	1 M $ZnSO_4$	[28]
Mo_6S_8	62 mA h g^{-1} at 60 mA g^{-1} 53 mA h g^{-1} at 0.6 A g^{-1}	55 mAh g^{-1} after 350 cycles at 0.6 A g^{-1}	1.1 M $ZnSO_4$	[29]
Al-doped	82.6 mA h g^{-1} at 80 mA	105 mAh g^{-1} after 50	1 M $ZnSO_4$	[30]

$VO_{1.52}(OH)_{0.77}$	g^{-1} 52.1 mA h g^{-1} at 0.56 A g^{-1}	cycles at 15 mA g^{-1}		
$Zn_xMo_6S_8$	134 mA h g^{-1} at 6.4 mA g^{-1} 53 mA h g^{-1} at 128 mA g^{-1}	88 mAh g^{-1} after 20 cycles at 6.4 mA g^{-1}	0.1 M $ZnSO_4$	[31]
Layered VS_2 Nanosheet	159.1 mA h g^{-1} at 100 mA g^{-1} 121 mA h g^{-1} at 1000 mA g^{-1}	110.9 mAh g^{-1} after 200 cycles at 500 mA g^{-1}	1 M $ZnSO_4$	[32]
Manganese Sesquioxide	137 mA h g^{-1} at 100 mA g^{-1} 38 mA h g^{-1} at 2000 mA g^{-1}	82.2 mAh g^{-1} after 1000 cycles at 2000 mA g^{-1}	2 M $ZnSO_4$	[33]
$Ni_xMn_{3-x}O_4$@C	139.7 mA h g^{-1} at 50 mA g^{-1} 98.5 mA h g^{-1} at 1200 mA g^{-1}	131 mAh g^{-1} after 850 cycles at 400 mA g^{-1}	2 M $ZnSO_4$ + 0.15 M $MnSO_4$	[34]

REFERENCES

[1] Wu S.; Wang W.; Li M.; Cao L.; Lyu F.; Yang M.; Wang Z.; Shi Y.; Nan B.; Yu S. Highly durable organic electrode for sodium-ion batteries via a stabilized α-C radical intermediate. *Nat. Commun.* **2016**, *7*, 13318.

[2] Lindström H.; Södergren S.; Solbrand A.; Rensmo H.; Hjelm J.; Hagfeldt A.; Lindquist S. Li^+ ion insertion in TiO_2 (Anatase). 2. voltammetry on nanoporous films. *J. Phys. Chem. B* **1997**, *101*, 7717.

[3] Brezesinski T.; Wang J.; Polleux J.; Dunn B.; Tolbert S. Templated nanocrystal-based porous TiO_2 films for next-generation electrochemical capacitors. *J. Am. Chem. Soc.* **2009**, *131*, 1802-1809.

[4] Niu C.; Meng J.; Wang X.; Han C.; Yan M.; Zhao K.; Xu X.; Ren W.; Zhao Y.; Xu L.; Zhang Q.; Zhao D.; Mai L. General synthesis of complex nanotubes by gradient electrospinning and controlled pyrolysis. *Nat. Commun.* **2015**, *6*, 1-9.

[5] Liu H.; Li C.; Zhang H.; Fu L.; Wu Y.; Wu H. Kinetic study on $LiFePO_4$/C nanocomposites synthesized by solid state technique. *J. Power Sources*, **2006**, *159*, 717-720.

[6] Xie J.; Kohno K.; Matsumura T.; Imanishi N.; Hirano A.; Takeda Y.; Yamamoto O. Li-ion diffusion kinetics in $LiMn_2O_4$ thin films prepared by pulsed laser deposition. *Electrochim. Acta.* **2008**, *54*, 376-381.

[7] Shaju K.; Subba Rao G.; Chowdari B. Li ion kinetic studies on spinel cathodes, Li $(M_{1/6}Mn_{11/6})O_4$ (M= Mn, Co, CoAl) by GITT and EIS. *J. Mater. Chem.* **2003**, *13*, 106-113.

[8] Hong J.; Selman J. Relationship between calorimetric and structural characteristics of Lithium - ion cells II. determination of Li transport properties. *J. Electrochem. Soc.* **2000**, *147*, 3190-3194.

[9] Kresse, G.; Joubert, D. From ultrasoft pseudopotentials to the projector augmented-wave method. *Phys. Rev. B* **1999**, *59*, 1758-1775.

[10] Perdew J.; Burke K.; Ernzerhof M. Generalized gradient approximation made simple. *Phys. Rev. Lett.* **1996**, *77*, 3865-3868.

[11] Blohl P. Phys. Rev. B: Condens. *Matter Mater. Phys.* **1994**, *50*, 17953–17979.

[12] Liechtenstein A.; Anisimov V.; Zaanen J. Density-functional theory and strong interactions: orbital ordering in Mott-Hubbard insulators. *Phys. Rev. B* **1995**, *52*, R5467-R5470.

[13] Li Y.; Wu M.; Ouyang C. The structural and electronic properties of spinel $MnCo_2O_4$ bulk and low-index surfaces: from first principles studies. *Appl. Surf. Sci.* **2015**, *349*, 510-515.

[14] Xu C.; Li B.; Du H.; Kang F. Energetic zinc ion chemistry: the rechargeable zinc ion battery. *Angew. Chem. Int. Ed.* **2012**, *51*, 933-935.

[15] Lee B.; Lee H.; Kim H.; Chung K.; Cho B.; Oh S. Elucidating the intercalation mechanism of zinc ions into α-MnO_2 for rechargeable zinc batteries. *Chem. Commun.* **2015**, *51*, 9265-9268.

[16] Lee J.; Ju J.; Cho W.; Cho B.; Oh S. Todorokite-type MnO_2 as a zinc-ion intercalating material. *Electrochim. Acta* **2013**, *112*, 138-143.

[17] Zhang L.; Chen L.; Zhou X.; Liu Z. Towards high-voltage aqueous metal-ion batteries beyond 1.5 V: the zinc/zinc hexacyanoferrate system. *Adv. Energy Mater.* **2015**, *5*, 1400930.

[18] Trócoli R., Mantia F. An aqueous zinc-ion battery based on copper hexacyanoferrate. *ChemSusChem* **2015**, *8*, 481-485.

[19] Alfaruqi M.; Mathew V.; Gim J.; Kim S.; Song J.; Baboo J.; Choi S.; Kim J. Electrochemically induced structural transformation in a γ-MnO_2 cathode of a high capacity zinc-ion battery system. *Chem. Mater.* **2015**, *27*, 3609-3620.

[20] Zhang N.; Cheng F.; Liu Y.; Zhao Q.; Lei K.; Chen C.; Liu X.; Chen J. Cation-deficient spinel $ZnMn_2O_4$ cathode in $Zn(CF_3SO_3)_2$ electrolyte for rechargeable aqueous Zn-ion battery. *J. Am. Chem. Soc.* **2016**, *138*, 12894-12901.

[21] Li G.; Yang Z.; Jiang Y.; Jin C.; Huang W.; Ding X.; Huang Y. Towards polyvalent ion batteries: a zinc-ion battery based on NASICON structured $Na_3V_2(PO_4)_3$. *Nano Energy* **2016**, *25*, 211-217.

[22] Chao D.; Zhu C.; Song M.; Liang P.; Zhang X.; Tiep N.; Zhao H.; Wang J.; Wang R.; Zhang H.; Fan H. A high-rate and stable quasi-solid-state zinc-ion battery with novel 2D layered zinc orthovanadate array. *Adv. Mater.* **2018**, *30*, 1803181.

[23] Wei T.; Li Q.; Yang G.; Wang C. High-rate and durable aqueous zinc ion battery using dendritic $V_{10}O_{24}\cdot 12H_2O$ cathode material with large interlamellar spacing. *Electrochim. Acta* **2018**, *287*, 60-67.

[24] Zhou J.; Shan L.; Wu Z.; Guo X.; Fang G.; Liang S. Investigation of V_2O_5 as a low-cost rechargeable aqueous zinc ion battery cathode. *Chem. Commun.* **2018**, *54*, 4457-4460.

[25] Cui J.; Wu X.; Yang S.; Li C.; Tang F.; Chen J.; Chen Y.; Xiang Y.; Wu X.; He Z. Cryptomelane-type KMn_8O_{16} as potential cathode material-for aqueous zinc ion battery. *Front. Chem.* **2018**, *6*, 352.

[26] Cai Y.; Liu F.; Luo Z.; Fang G.; Zhou J.; Pan A.; Liang S. Pilotaxitic $Na_{1.1}V_3O_{7.9}$ nanoribbons/graphene as high-performance sodium ion battery and aqueous zinc ion battery cathode. *Energy Storage Mater.* **2018**, *13*, 168-174.

[27] Ko J.; Sassin M.; Parker J.; Rolison D.; Long J. Combining battery-like and pseudocapacitive charge storage in 3D MnO_x@ carbon electrode architectures for zinc-ion cells. *Sustainable Energy Fuels* **2018**, *2*, 626-636.

[28] Yang S.; Zhang M.; Wu X.; Wu X.; Zeng F.; LiY.; Duan S.; Fan D.; Yang Y.; Wu X. The excellent electrochemical performances of $ZnMn_2O_4/Mn_2O_3$: the composite cathode material for potential aqueous zinc ion batteries. *J. Electroanal. Chem.* **2019**, *832*, 69-74.

[29] Cheng Y.; Luo L.; Zhong L.; Chen J.; Li B.; Wang W.; Mao S.; Wang C.; Sprenkle V.; Li G.; Liu J. Highly reversible zinc-ion intercalation into chevrel phase Mo_6S_8 nanocubes and applications for advanced zinc-ion batteries. *ACS Appl. Mater. Inter.* **2016**, *8*, 13673-13677.

[30] Jo J.; Sun Y.; Myung S. Hollandite-type Al-doped $VO_{1.52}(OH)_{0.77}$ as a zinc ion insertion host material. *J. Mater. Chem. A* **2017**, *5*, 8367-8375.

[31] Chae M.; Heo J.; Lim S.; Hong S. Electrochemical zinc-ion intercalation properties and crystal structures of $ZnMo_6S_8$ and $Zn_2Mo_6S_8$ chevrel phases in aqueous electrolytes. *Inorg. Chem.* **2016**, *55*, 3294-3301.

[32] He P.; Yan M.; Zhang G.; Sun R.; Chen L.; An Q.; Mai L. Layered VS_2 nanosheet-based aqueous Zn ion battery cathode. *Adv. Energy Mater.* **2017**, *7*, 1601920.

[33] Jiang B.; Xu C.; Wu C.; Dong L.; Li J.; Kang F. Manganese sesquioxide as cathode material for multivalent zinc ion battery with high capacity and long cycle life. *Electrochim. Acta* **2017**, *229*, 422-428.

[34] Long J.; Gu J.; Yang Z.; Mao J.; Hao J.; Chen Z.; Guo Z. Highly porous, low band-gap $Ni_xMn_{3-x}O_4$ ($0.55 \leq x \leq 1.2$) spinel nanoparticles with in situ coated carbon as advanced cathode materials for zinc-ion batteries. *J. Mater. Chem. A* **2019**, *7*, 17854-17866.